ESTIMATION OF THE DISCRETE SPECTRUM OF RELAXATIONS FOR ELECTROMAGNETIC INDUCTION RESPONSES

A Thesis
Presented to
The Academic Faculty

by

Mu-Hsin Wei

In Partial Fulfillment
of the Requirements for the Degree
Master of Science in the
School of Electrical and Computer Engineering

Georgia Institute of Technology
May 2011

To my loving parents.

ACKNOWLEDGEMENTS

I thank God. His love never fails. Through Him, new things are born and new lives begin. The creativity that shaped this work belongs to Him.

I am thankful for my advisers Dr. McClellan and Dr. Scott, for their patient guidance and valuable input. I would like to thank Dr. McClellan, who provided direction and encouragement. Most especially, I appreciate his care for the learning and development of students. I would like to thank Dr. Scott, who meticulously guided me since the beginning of the project. Many significant results from this thesis originated from his ideas. I consider it a great privilege to work under the supervision of Dr. McClellan and Dr. Scott, to whom I am deeply grateful.

I would like to thank my parents, who always support me and welcome me. I thank my sister Lily for her frequent encouragement and phone calls. I also acknowledge Tim and Sean, who although are far away but are close to heart.

I would also like to thank my friends and colleagues, for their friendship and support. Much of the credit of this work goes to these fantastic people. I especially like to thank my housemates, Jacob, Justin, and David, who kept me sane and positive.

This work is supported in part by the US Army REDCOM CERDEC Night Vision and Electronic Sensors Directorate, Science and Technology Division, Countermine Branch and in part by the U. S. Army Research Office under Contract Number W911NF-05-1-0257.

TABLE OF CONTENTS

LIST OF TABLES

LIST OF FIGURES

SUMMARY

This thesis presents a robust method for estimating the relaxations of a metallic object from its electromagnetic induction (EMI) response. The EMI response of a metallic object can be accurately modeled by a sum of real decaying exponentials. However, it is difficult to obtain the model parameters from measurements when the number of exponentials in the sum is unknown or the terms are strongly correlated. Traditionally, the time constants and residues are estimated by nonlinear iterative search that often leads to unsatisfactory results.

In this thesis, a constrained linear method of estimating the parameters is formulated by enumerating the relaxation parameter space and imposing a nonnegative constraint on the parameters. The resulting algorithm does not depend on a good initial guess to converge to a solution. Using tests on synthetic data and laboratory measurement of known targets the proposed method is shown to provide accurate and stable estimates of the model parameters.

CHAPTER I

INTRODUCTION

The landmine crisis remains today as landmines continue to maim or kill civilians everyday worldwide. The International Campaign to Ban Landmines reported that in the year of 2009, landmines and explosive remnants of war caused about 4000 casualties worldwide, of which over 60% are civilians [19] and more than 30% are children. Much effort and research has been invested in remediating landmines with one of the primary tasks being the detection of the landmine itself. However, landmine detection can suffer from a high false-alarm rate as the detectors also detect other metallic non-mine objects like gun shells, metal cans, and shrapnel. Therefore, it is of strong interest to discriminate between landmines and metallic non-mine objects.

Recent research has shown that discrimination between certain types of metallic objects (targets) is possible by using broadband electromagnetic induction (EMI) sensors together with advanced signal processing [6, 21, 11, 27, 9, 26]. Target discrimination using broadband EMI sensors is possible because the EMI response of a target is strongly related to the target's physical size, shape, orientation, and composition. EMI sensors work by illuminating a target of interest with a time-varying magnetic field, and then detecting the scattered magnetic field which is generated by the eddy currents induced on the target. The broadband EMI sensors measure the scattered field at a broad range of frequencies or measurement times. In a broadband EMI system, a target can be represented by its response at a small number of frequencies. The measured response can be fitted to a model, and discrimination of the target is performed based on the fitted model parameters.

The goal of this work is to model an EMI response in terms of its relaxations to assist target discrimination. Several different EMI models have been developed to analyze the EMI response of a target. These models can be categorized into two: continuous and discrete. While this thesis is concerned with the discrete model, the continuous model is

used by many [9, 26], and a discussion on this model is also provided.

1.1 Continuous Distribution of Relaxations

Several existing EMI models can be identified with parametric models employed in polymer science, which have an underlying continuous distribution of relaxations. For example, the parametric models proposed by Miller *et al.* [24] (which is widely used) can be rewritten in the form of the Cole-Cole dielectric relaxation model [5]. Other theoretical model for canonical targets can also be identified similarly [13, 35].

The fact that the dielectric response of materials has similar characteristics to the EMI frequency response allows the models and methods developed for dielectric materials be applied to the EMI response. Here, the analysis used in polymer science is employed to study some of the existing EMI models. It is advantageous to do so since many of the dielectric models and methods have been well-studied over the past fifty years, and much is known about the behavior and properties of the models. Other well-known dielectric models, such as the Havriliak-Negami and Cole-Davidson models could also be used in modeling the EMI response of targets with more complex shapes [8, 16].

A more general model to describe the models mentioned above is the distribution of relaxation times (DRT), which is an analysis tool used in polymer science to characterize materials [18]. The normalized DRT $G(\tau)$ is defined as:

$$H(\omega) = g_0 + g_\Delta \int_0^\infty \frac{G(\tau)}{1 + j\omega\tau} \mathrm{d}\tau, \tag{1}$$

where $H(\omega)$ is the frequency response, τ the relaxation time, and g_0 and g_Δ are constants; $G(\tau)$ is normalized to have unity area.

The models mentioned above can all be expressed in terms of the DRT. For example, the Cole-Cole model (hence, Miller's model) and its DRT are [1]

$$H_{CC}(\omega) = g_0 + \frac{g_\Delta}{1 + (j\omega\tau_0)^\alpha}, \tag{2}$$

and

$$G_{CC}(\tau) = \frac{1}{2\pi\tau} \frac{\sin(\alpha\pi)}{\cosh(\alpha \log(\tau/\tau_0)) + \cos(\alpha\pi)}, \tag{3}$$

where τ_0 and α are model parameters.

It should be noted that the parametric models can be restrictive in the sense that the models have assumed underlying distribution and may not be appropriate for objects of more general shape. For example, $G_{CC}(\tau)$ is restricted to be symmetric with respect to τ_0 in log-τ space because of the assumed structure of $H_{CC}(\omega)$. However, not all targets have symmetric DRTs. Using Cole-Cole to model such targets would result in a loss of information. Describing a target in terms of DRT makes less assumptions about the structure of the response, and therefore can model different targets more accurately.

1.2 Discrete Spectrum of Relaxation Frequencies

In the study of EMI, several researchers have provided a theoretical basis for representing the EMI response of a metallic object as a discrete sum of damped real exponentials [20, 2]. In terms of the DRT, an EMI response can be modeled as a special case of the DRT where the $G(\tau)$ is *discrete*. In addition, in the context of broadband EMI application, it is more intuitive and convenient to write (1) in terms of *relaxation frequencies* rather than relaxation times. Using the notation of relaxation frequency, (1) can be rewritten in discrete form as

$$H(\omega) = c_0 + \sum_{k=1}^{K} \frac{c_k}{1 + j\omega/\zeta_k}, \tag{4}$$

where c_0 is the shift, K the model order, c_k the real spectral amplitudes, and $\zeta_k = 1/\tau_k$ the relaxation frequencies. The underlying physical process of the model is discussed in Appendix A. The response at zero frequency $H(0) = \sum_{k=0}^{K} c_k$ is due to the DC magnetization of the target.

Aside from the shift, the EMI frequency response of a target can be precisely represented by the set $S = \{(\zeta_k, c_k) : k = 1 \dots K\}$ which is the discrete spectrum of relaxation frequencies (DSRF). Each pair (ζ_k, c_k) is one relaxation. The parameter c_0 is not considered part of the DSRF because it is just a shift of the frequency response. The term DSRF and spectrum are used interchangeably in this work.

The DSRF is related to a target's physical properties. The frequency response $H(\omega)$ is proportional to the projection of the magnetic polarizability tensor of the target being measured by the EMI sensor. The magnetic polarizability, hence the DSRF, of several canonical targets can be calculated analytically, and these formulas show how the DSRF

is related to the target's physical properties such as conductivity, permeability, shape, size, and orientation [34, 3, 12].

The DSRF representation has other useful properties. The relaxation frequencies of a target are invariant to its relative orientation and position to the sensor. Only the spectral amplitudes change with orientation and position. The fact that the relaxation frequencies are intrinsic to a target makes the DSRF a valuable feature for target discrimination. Baum has coined the term "magnetic singularity identification" when using the relaxations (singularities) for identifying targets [3].

1.3 DSRF Modeling Difficulties

While modeling the EMI response in terms of the DSRF has several benefits, estimating the DSRF from the frequency response is not straightforward. Estimating the DSRF is equivalent to finding the parameters of a sum of exponentials, and techniques such as iterative nonlinear least squares fitting, the matrix pencil method, and modified Prony's methods have been used in the past [29, 25]. Often these methods do not perform well when three or more relaxations are present. The goodness of fit strongly depends on a good guess of the model order, and is also very sensitive to the initial guess for the model parameters. More discussion on the performance of these methods can be found in [27, 7].

In practice, a good initial guess is hard to determine, and it is difficult, if not impossible, to have prior knowledge on the model order. For these reasons, most existing estimation methods are prone to not converging in the fitting process. Even if the fitting method converges well with a small residual, there is the concern that the estimated relaxations could be very different from the actual ones. It is possible that the estimate is merely a good numerical fit, but has no physical significance [7].

One robust spectrum estimation method is the MATLAB function `invfreqs` which implements the algorithm proposed by Levy [23]. `invfreqs` is robust in the sense that it can accurately estimate the spectrum of three or more relaxations, and its convergence is not sensitive to the initial guess. The major downside of this method is that it can return complex spectral amplitudes or negative relaxation frequencies that have no physical

meaning.

1.4 Proposed Method

In this thesis, it is proposed a method of estimating the DSRF that requires no prior knowledge of the model order and always returns real model parameters. The proposed method linearize the estimation problem by enumerating the relaxation parameter space and imposing a nonnegative constraint on the parameters [37]. While some targets may have negative DSRF, the proposed method works very well in practice. Even with the constraint, the proposed method can represent a much larger class of responses than the parametric models such as the Cole-Cole and Havriliak-Negami models. For well-known canonical targets, as presented in this work, the estimated DSRF is an approximate, if not an exact, representation of the actual physical DSRF.

CHAPTER II

ESTIMATION METHOD

The proposed DSRF estimation method is formulated in this chapter. To begin the formulation, it is first examined the frequency response when probed at multiple frequencies. When the target response is measured at N distinct frequencies, the DSRF model (4) can be written in matrix form

$$\begin{bmatrix} H(\omega_1) \\ H(\omega_2) \\ \vdots \\ H(\omega_N) \end{bmatrix} = \underbrace{\begin{bmatrix} 1 & \frac{1}{1+j\omega_1/\zeta_1} & \frac{1}{1+j\omega_1/\zeta_2} & \cdots & \frac{1}{1+j\omega_1/\zeta_K} \\ 1 & \frac{1}{1+j\omega_2/\zeta_1} & \frac{1}{1+j\omega_2/\zeta_2} & \cdots & \frac{1}{1+j\omega_2/\zeta_K} \\ \vdots & \vdots & \vdots & \ddots & \vdots \\ 1 & \frac{1}{1+j\omega_N/\zeta_1} & \frac{1}{1+j\omega_N/\zeta_2} & \cdots & \frac{1}{1+j\omega_N/\zeta_K} \end{bmatrix}}_{\boldsymbol{Z}} \begin{bmatrix} c_0 \\ c_1 \\ c_2 \\ \vdots \\ c_K \end{bmatrix}$$

$$\boldsymbol{h} = \boldsymbol{Z}\boldsymbol{c}, \tag{5}$$

where $\omega_{min} = \omega_1 < \omega_2 < \cdots < \omega_N = \omega_{max}$, $\boldsymbol{h}$ is the observation vector, $\boldsymbol{c}$ the spectral amplitude vector augmented by the shift c_0, and $\boldsymbol{Z}$ a matrix containing information about the relaxation frequencies $\boldsymbol{\zeta}$. The dimension of the matrix $\boldsymbol{Z}$ is dependent on the number of relaxations present in the spectrum (i.e., the model order). In the case of a simple thin wire circular loop, there is only one relaxation, so $\boldsymbol{Z}$ has two columns; the first column is always one to account for c_0.

2.1 Method Formulation

To estimate the DSRF (i.e., ζ_k and c_k) from a given observation $\boldsymbol{h}$, the usual approach is to minimize the norm of the error, $\|\boldsymbol{h} - \boldsymbol{Z}\boldsymbol{c}\|$, but this leads to a *nonlinear* optimization problem. Instead, the strategy of basis pursuit is adopted to reformulate (5) as a linear problem with an overcomplete dictionary [4], and then nonnegative least squares is used to select the best basis, i.e., the best $\boldsymbol{\zeta}$. The overcomplete dictionary is a matrix $\tilde{\boldsymbol{Z}}$ that has the same form as $\boldsymbol{Z}$ in (5), but with many more column (shown below). To generate

the columns, it is enumerated a large set of possible relaxation frequencies in log-ζ space, and one column is created for each enumerated ζ. The enumeration is done by discretizing a range of relaxation frequencies into M sample points $\tilde{\zeta}_m$ that are uniformly distributed in the log-ζ space. The range of relaxation frequencies is chosen such that, $\tilde{\zeta}_{min} \approx \omega_{min}$ and $\tilde{\zeta}_{max} \approx \omega_{max}$. The number M should be chosen large enough to ensure some $\tilde{\zeta}_m$ are in close proximity to the actual relaxation frequencies ζ_k. From simulations performed, a good choice of M gives roughly 25 sample points per decade. More discussion on the choice of M can be found in Appendix C.

Using the dictionary $\tilde{\boldsymbol{Z}}$, the estimation problem is rewritten as

$$\begin{bmatrix} H(\omega_1) \\ H(\omega_2) \\ \vdots \\ H(\omega_N) \end{bmatrix} = \underbrace{\begin{bmatrix} 1 & \frac{1}{1+j\omega_1/\tilde{\zeta}_1} & \frac{1}{1+j\omega_1/\tilde{\zeta}_2} & \cdots & \frac{1}{1+j\omega_1/\tilde{\zeta}_M} \\ 1 & \frac{1}{1+j\omega_2/\tilde{\zeta}_1} & \frac{1}{1+j\omega_2/\tilde{\zeta}_2} & \cdots & \frac{1}{1+j\omega_2/\tilde{\zeta}_M} \\ \vdots & \vdots & \vdots & \ddots & \vdots \\ 1 & \frac{1}{1+j\omega_N/\tilde{\zeta}_1} & \frac{1}{1+j\omega_N/\tilde{\zeta}_2} & \cdots & \frac{1}{1+j\omega_N/\tilde{\zeta}_M} \end{bmatrix}}_{\tilde{\boldsymbol{Z}}} \begin{bmatrix} \tilde{c}_0 \\ \tilde{c}_1 \\ \tilde{c}_2 \\ \vdots \\ \tilde{c}_M \end{bmatrix} + error$$

$$\boldsymbol{h} = \tilde{\boldsymbol{Z}}\tilde{\boldsymbol{c}} + error \tag{6}$$

where $\tilde{\boldsymbol{c}}$ is the (M+1)-element *weighted selector vector*. Ideally, when the error between $\boldsymbol{h}$ and $\tilde{\boldsymbol{Z}}\tilde{\boldsymbol{c}}$ is minimized, only those $\tilde{c}_m$ with corresponding $\tilde{\zeta}_m$ that are near a true ζ_k will be nonzero, and they will take on the correct spectral amplitudes c_k. It follows that a DSRF can then be deduced from the nonzero estimated $\tilde{c}_m$ and their corresponding $\tilde{\zeta}_m$. It is expected that a good solution for $\tilde{\boldsymbol{c}}$ has many zero elements.

The challenge in obtaining the correct $\tilde{\boldsymbol{c}}$ is that M is much greater than N, so the system in (6) is underdetermined and there is not a unique $\tilde{\boldsymbol{c}}$ to minimize the error. Any vector in the null space of $\tilde{\boldsymbol{Z}}$ can be added to $\tilde{\boldsymbol{c}}$ without changing the error. There are many ways to select a least-squares (LSQ) solution. The Moore-Penrose pseudoinverse picks the LSQ solution that has the smallest ℓ_2 norm. One can also compute a LSQ solution with the fewest nonzero components. However, neither of these LSQ solutions produces the correct spectrum. Details about existing techniques and the difficulties of solving such a system can be found in [15, 7, 17].

In the EMI application, it is found in this research that imposing a nonnegative constraint on $\tilde{\boldsymbol{c}}$ effectively eliminates a large portion of the null space of $\tilde{\boldsymbol{Z}}$ and the remaining solution space contains reasonable answers. Under the EMI system used in this study, it is observed that the real part of the frequency response decreases as the frequency increases, and the imaginary part remains negative for the great majority of targets. Having all the spectral amplitudes nonnegative is a sufficient condition to satisfying this observation. While it is shown that nonnegative DSRF is not a necessary condition, it is also shown that whenever the real part decreases with respect to the frequency, the spectral amplitudes are practically nonnegative. A detailed discussion on the applicability of the nonnegative constraint is provided in Appendix B.

Using the nonnegative constraint, 6 can be solved by optimizing

$$\arg\min_{\tilde{\boldsymbol{c}}} ||\tilde{\boldsymbol{Z}}'\tilde{\boldsymbol{c}} - \boldsymbol{h}'|| \qquad \text{subject to } \tilde{\boldsymbol{c}} \geq 0 \tag{7}$$

$$\text{where } \tilde{\boldsymbol{Z}}' = \begin{bmatrix} \mathfrak{Re}(\tilde{\boldsymbol{Z}}) \\ \mathfrak{Im}(\tilde{\boldsymbol{Z}}) \end{bmatrix} \text{ and } \boldsymbol{h}' = \begin{bmatrix} \mathfrak{Re}(\boldsymbol{h}) \\ \mathfrak{Im}(\boldsymbol{h}) \end{bmatrix}.$$

Separating the real and imaginary parts makes the whole system real. The first element in $\tilde{\boldsymbol{c}}$, $\tilde{c}_0$, can be guaranteed nonnegative by adding a sufficiently large real number to $\boldsymbol{h}$.

2.2 Implementation

The proposed estimation method can be easily implemented through the function `lsqnonneg` in MATLAB which uses the algorithm found in [22]. An alternative to `lsqnonneg` is the `CVX` package which implements convex optimization under MATLAB [14]. Both optimizers provides satisfactory results. However, `CVX` is a larger and more sophisticated program, but is slightly slower than `lsqnonneg` which was written exactly to solve least-square problems with a nonnegative constraint. Nevertheless, `CVX` would be of great interest if more constraints are to be added.

When using either `lsqnonneg` or `CVX`, it is found that normalizing the input data $\boldsymbol{h}$ to have an ℓ_2 norm of unity increases the accuracy of estimation. Therefore, all data are scaled to an ℓ_2 norm of unity before optimization, and scaled back to the original norm after optimization. The original norm may contain useful information for target discrimination.

2.3 Interpolation

It is observed that in the estimated DSRF, an expected relaxation (ζ_{true}, c_{true}) is often split into two peaks located at the two sample points adjacent to ζ_{true}, as shown in Fig. 1. It is also observed that the two estimated spectral amplitudes add up to the true spectral amplitude c_{true}, and ζ_{true} is closer to the $\tilde{\zeta}$ with larger $\tilde{c}$. This phenomenon can be understood: the splitting of relaxation happens when the sample points $\tilde{\zeta}_m$ do not coincide with ζ_{true}, and c_{true} gets distributed among the two sample points that are the closest to ζ_{true}.

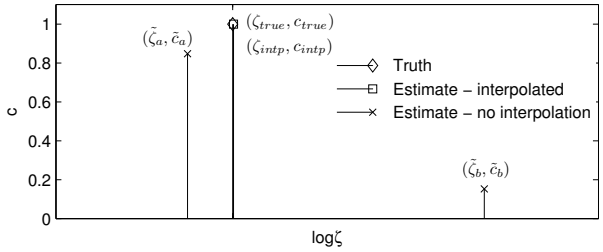

Figure 1: Splitting of an expected relaxation followed by interpolation. The sample points $\tilde{\zeta}$ do not coincide with ζ_{true}, so ζ_{true} is split into the two nearest sample points: $\tilde{\zeta}_a$ and $\tilde{\zeta}_b$. The estimation accuracy is increased by interpolating in $\tilde{\zeta}$ using $\tilde{c}_a$ and $\tilde{c}_b$.

The accuracy of the estimation can be increased by taking advantage of this well-behaved and consistently recurring phenomenon. The splitting processes can be reversed. A true relaxation frequency could be restored by interpolating between two adjacent $\tilde{\zeta}_m$ with nonzero $\tilde{c}_m$ according to their spectral amplitudes. The interpolated spectral amplitude is simply the sum of the two adjacent spectral amplitudes. Mathematically,

$$c_{intp} = \tilde{c}_a + \tilde{c}_b \tag{8}$$

$$\log(\zeta_{intp}) = \log(\tilde{\zeta}_a) + \frac{\tilde{c}_b}{\tilde{c}_a + \tilde{c}_b} \log(\tilde{\zeta}_b/\tilde{\zeta}_a). \tag{9}$$

The quantities are as depicted in Fig. 1. The sample points $\tilde{\zeta}_m$ are placed close enough that a simple linear interpolation in log-ζ space gives satisfactory results. The interpolation is applied only on two adjacent nonzero relaxations.

After the interpolation is performed, any $\tilde{c}_m$ with a value of zero is eliminated along with its corresponding $\tilde{\zeta}_m$. The resulting relaxation frequencies is denoted as $\hat{\zeta}_l$, with spectral amplitudes, $\hat{c}_l$, or in vector notation, $\hat{\boldsymbol{\zeta}}$ and $\hat{\boldsymbol{c}}$, both with length L. It is convenient and

desirable to interpret the estimation results by looking at $\hat{\boldsymbol{\zeta}}$ and $\hat{\boldsymbol{c}}$. Every entry in $\hat{\boldsymbol{\zeta}}$ is an estimate of one relaxation frequency of the target with its corresponding estimated spectral amplitude in $\hat{\boldsymbol{c}}$. The estimated DSRF $\hat{S} = \{(\hat{\zeta}_l, \hat{c}_l) : l = 1 \dots L\}$ is then compactly stored in $\hat{\boldsymbol{\zeta}}$ and $\hat{\boldsymbol{c}}$. In addition, the vector length L is an estimate of the model order K. Note that $\tilde{c}_0$ is not part of the DSRF and therefore not interpolated, and is not in the vector $\hat{\boldsymbol{c}}$.

2.4 Summary

To estimate the unknown DSRF $S = \{(\zeta_k, c_k)\}$ from a given set of observations $\boldsymbol{h}$ over N frequencies, first decide on a relaxation frequency range $[\tilde{\zeta}_{min}, \tilde{\zeta}_{max}]$ and the number of points M to be sampled in this range. Then generate the sample points $\tilde{\zeta}_m$, construct a dictionary matrix $\tilde{\boldsymbol{Z}}$, perform the optimization described in (7), and finally obtain the estimated DSRF $\hat{S} = \{(\hat{\zeta}_l, \hat{c}_l)\}$ by interpolating the solution $\tilde{\boldsymbol{c}}$ returned by the optimizer.

The performance of the proposed method is discussed in detail in the following chapter.

CHAPTER III

ESTIMATION PERFORMANCE

To examine the performance of the proposed method, the method is tested against synthetic, laboratory, and field data. The method is shown to be accurate, stable, and fast. All estimations are performed with $M = 100$ and optimized with `lsqnonneg`. Prior to presenting the estimation results, an error measure is introduced.

In assessing the signal strength, the signal-to-noise ratio (SNR) is used. The signal power is computed by $\sum_{i=1}^{N} |H(\omega_i)|^2/N$. The noise power in synthesized data is equal to the variance of the noise. In laboratory and field data the background signal can be measured and is treated as noise when calculating the SNR.

The frequency response of targets are presented on Argand diagrams. Specifically, complex frequency response functions are plotted on a complex plane with the imaginary part as the vertical axis, the real part as the horizontal axis, and frequency as the parameter. All presented spectra are normalized such that $\sum_{i=1} c_i = 1$ (c_0 is separate). Normalization removes the influence of the signal amplitude which changes for many reasons.

Notation: ζ and c are the true/theoretical relaxation frequencies and spectral amplitudes; $\hat{\zeta}$ and $\hat{c}$ are the estimates.

3.1 Dissimilarity Measure Between Two DSRFs

Before the goodness of estimation can be evaluated, some kind of measure is needed to assess the dissimilarity between the estimated DSRF and the truth. It is difficult, however, to compare two sparse spectra when the number of relaxations are different, which happens frequently. When the number of relaxations is the same (K=L), a possible measure of the dissimilarity between two spectra is

$$D(\hat{S}, S) = \frac{1}{I} \sum_{i=1}^{I} |\log \hat{\zeta}_i - \log \zeta_i| \tag{10}$$

$$\forall\, i \quad \hat{\zeta}_i \leq \hat{\zeta}_{i+1} \text{ and } \zeta_i \leq \zeta_{i+1},$$

where I=K=L. In (10) only the relaxation frequencies ζ_k are considered, and spectral amplitudes c_k are ignored. This approximation is reasonable and convenient when two spectra are visually similar. We refer to this dissimilarity measure as the deviation. It has the units of decades.

Another measure that is more comprehensive is the Earth Mover's Distance (EMD) [28, 10]. The EMD consistently quantifies the dissimilarity between two spectra, even when $K \neq L$. Intuitively, the EMD measures how much work it takes to morph one spectrum into the other. Specifically, one spectrum represents piles of earth with volume $\hat{c}_l$ located at the associated $\hat{\zeta}_l$. The other spectrum represents holes in the ground with capacity c_k located at ζ_k. The distance between a pile of earth and a hole is naturally defined to be the difference between $\hat{\zeta}_l$ and ζ_k in log space, and the work to move some earth into a hole would be the amount of earth moved times the distance traveled. Then, the EMD is proportional to the least amount of work needed to move as much earth into the holes. For the DSRF, the EMD is measured in decades because it is almost always examined in log-ζ space. See Appendix E for details about the EMD.

3.2 Synthetic Data

In this section, the proposed estimation method is tested against synthetic data to show its functionality, robustness, and stability. The synthesized data is sampled at 21 frequencies approximately logarithmically distributed over the range 300 Hz–90 kHz. The range of ζ for estimation is chosen such that $\log(\tilde{\zeta}_{min})$ and $\log(\tilde{\zeta}_{max})$ are 2.4470 and 6.6223, respectively. This corresponds to a frequency range of 45 Hz–670 kHz, which is larger than the measured frequency range. With $M = 100$, the spacing between two sample points is 0.0422 decades. The number of samples and the frequencies are chosen to be the same as the laboratory hardware system, but the proposed method can also perform under different settings.

3.2.1 Two Coplanar Coaxial Loops

The performance of the proposed method is good when tested on a simulated two coplanar coaxial circular loops of copper wire. The two loops have circumferences 200 mm and

150 mm, respectively. The larger loop has a wire radius of 0.0635 mm (#36 AWG[1]), and the smaller one a wire radius of 0.3215 mm (#22 AWG). A theoretical EMI response and the DSRF of this target is provided in Appendix D. The EMI response is simulated at a 70 dB signal-to-noise ratio (SNR) with additive white Gaussian noise (AWGN). The estimated spectrum is shown in Fig. 2 along with the true spectrum. The estimated spectrum is almost identical to the truth. The deviation from the true spectrum is 0.0013 decades, which is very small compared to the detectable ζ range, about 4 decades. The computation took 0.11 s on a 2.66 GHz CPU with 960 MB RAM.

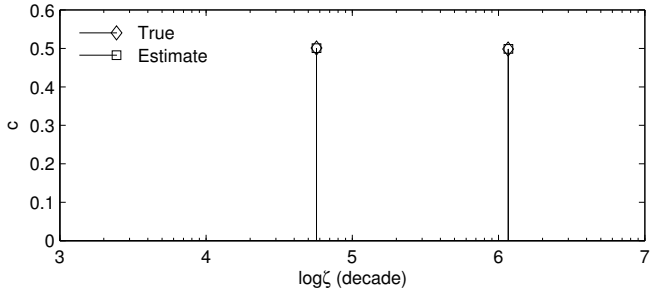

Figure 2: Estimation of a simulated two coplanar coaxial circular loop target, for which $\log\zeta_k$ and c_k are (4.7552 6.0651) and (0.5013 0.4987), respectively. The estimates for $\log\hat{\zeta}_l$ and $\hat{c}_l$ are (4.7557 6.0672) and (0.5010 0.4990), respectively.

3.2.2 Six-relaxation DSRF

While existing sum-of-exponentials estimation methods can also successfully estimate a two-relaxation case, when the number of relaxations is three or more, these methods start to encounter problems such as returning complex model parameters or not converging [7]. Here, the proposed method is tested on a six-relaxation DSRF. The target response is synthesized at 70 dB SNR with AWGN:

$$H(\omega) = 1 + \sum_{k=1}^{6} \frac{c_k}{1 + j\omega/\zeta_k} + noise. \tag{11}$$

The relaxation frequencies are chosen such that two ζ_k coincide with a sample point, one ζ_k is half way between two log-ζ sample points, and the rest are randomly in between sample points. The relaxation frequencies are chosen this way to demonstrate the functionality

[1] American wire gauge

of the proposed method when the sample points do not coincide with the true relaxation frequencies.

The synthesized and estimated DSRFs are shown in Fig. 3(a) and Table 1. All six relaxation frequencies are correctly recovered. The estimated model parameters are real, and the deviation from truth is small. The EMD between the estimate and truth is 0.0365 decades. There is a seventh relaxation in the estimate introduced by the noise, but its spectral amplitude is small.

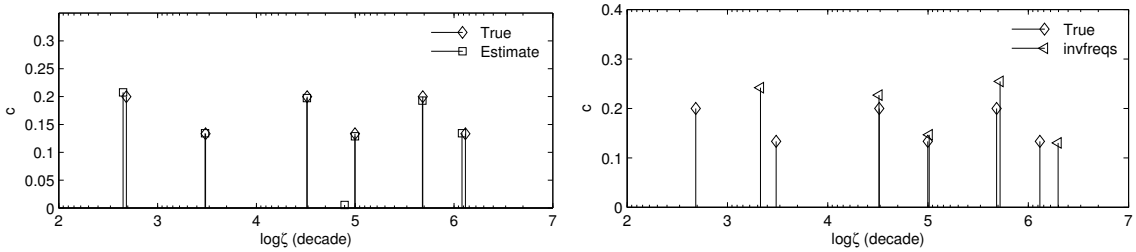

(a) (b)

Figure 3: Estimation of a six-relaxation DSRF. See Table 1 for numerical data. (a) Estimates by the proposed method. (b) Estimates by `invfreqs` with nonphysical parameters removed.

The same DSRF is also estimated using `invfreqs`. The a priori model order is chosen to be 8 which is slightly higher than the actual but is reasonable because in practice it is difficult to know the actual model order. The estimated model parameters are recorded in Table 1. There are two estimated ζ that are complex and one negative. A physically possible DSRF can be obtained by throwing away these complex or negative relaxation frequencies. The resulting estimated DSRF is shown in Fig. 3(b). Three relaxations are correctly recovered, but the two left most expected relaxations are not. The EMD between the estimate and truth is 0.3323 decades, much higher than the EMD of the proposed method.

Table 1: Estimation of a six-relaxation DSRF

Truth	c_k	0.2000	0.1333	0.2000	0.1333	0.2000	0.1333			
	$\log \zeta_k$	2.6842	3.4855	4.5135	4.9985	5.6839	6.1162			
Proposed method	$\hat{c}_l$	0.2076	0.1343	0.1973	0.1286	0.1928	0.1341	0.0052		
	$\log \hat{\zeta}_l$	2.6515	3.4803	4.5109	4.9981	5.6801	6.0809	4.8931		
`invfreqs`	$\hat{c}_l$		0.2418	0.2269	0.1465	0.2546	0.1301	$-0.3902 \cdot 10^{-4}$	$-0.3902 \cdot 10^{-4}$	0.1334
	$\log \hat{\zeta}_l^{\dagger}$		3.3303	4.5111	5.0126	5.7188	6.2983	$-0.0012 + 0.0042i$	$-0.0012 - 0.0042i$	-0.0127

†Negative or complex values are not logged

Although a physically possible DSRF can be obtained by throwing away the nonphysical estimates, the resulting spectrum can be quite different from the truth. Using the actual model order or its neighboring numbers as the a priori model order does not preclude complex model parameters either. Nevertheless, when the true model order is low and the SNR is high, satisfactory estimates can be obtained from `invfreqs` by throwing out nonphysical parameters.

Returning complex or nonphysical estimates is a problem that plagues many methods, and there is not a proper way to deal with the complex estimates. The best way is perhaps to restrict the model parameters to be real and physical when setting up the problem, and this is the approach taken in the proposed method.

3.2.3 Signal to Noise Ratio

To see how the proposed method performs in noise, a Monte Carlo simulation versus SNR is run on a target with a four-relaxation DSRF. Goodness of estimation is measured by the EMD between the estimate and truth. The simulation result, shown in Fig. 4, shows the robustness of the estimation method at different signal-to-noise ratios.

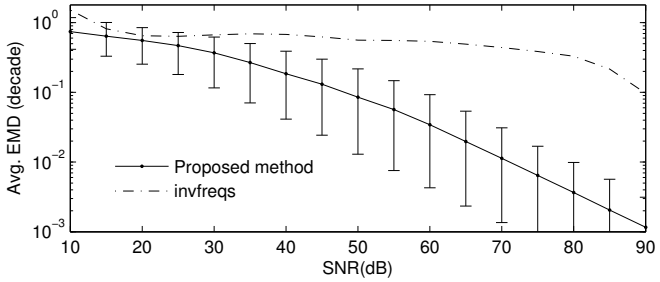

Figure 4: Monte Carlo simulation on goodness of estimation vs. SNR performed on a four-relaxation DSRF. Sample size is 10,000 at each SNR. Error bars indicate the range of EMD between the 10th and 90th percentiles.

As expected, the EMD between the estimate and the truth increases as the SNR decreases. This suggests that the proposed method is functional in a range of SNR where the EMD is below some threshold. This threshold, however, depends on the application of the estimated spectrum. For example, in the case of classification, a more robust classifier may tolerate worse estimations and, therefore, allow lower SNR.

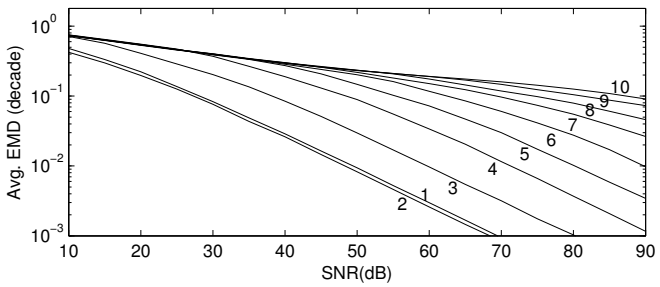

Figure 5: Monte Carlo simulation on goodness of estimation vs. SNR for different DSRFs with model order ranging from 1 to 10. Sample size is 10,000.

The same noise simulation was also performed on `invfreqs` using the actual model order as the a priori model order. Nonphysical parameters are removed from the estimate. As shown in Fig. 4, `invfreqs` barely functions except at around 90 dB SNR where its average EMD drops to 0.1 decades. In comparison, the proposed method has an average EMD one hundred times smaller than that of `invfreqs` at 90 dB SNR, and has low EMD for a wide range of SNR.

Figure 5 shows the same Monte Carlo simulation performed on DSRFs with different model orders using the proposed method. It is seen that a higher model order DSRF requires a higher SNR to achieve a given goodness of fit (EMD). Although the curves are different for each model order, all curves have the same behavior, i.e., the goodness of estimation is positively correlated to the SNR. The consistent trend of these curves suggests that the proposed method is stable and functional over a wide range of SNR.

While it seems rather high the SNR levels at which the simulations were conducted, it was observed that what would usually be a high SNR in other applications is noisy for the EMI application. For example (Fig. 6), a frequency response added with a 25 dB AWGN appears noisy even though a 25 dB AWGN would be considered as a very high SNR in other applications, like radar. In addition, the range of the SNR for the simulation was chosen to be close to what is observed in practice. In the laboratory measurements, a typical SNR for loop targets in this work is 70 dB when the target is placed 10 cm below the EMI sensor. In reality, the depth and size of the target are two dominant factors of SNR. The SNR increases with the size of the target, and decreases with the buried depth.

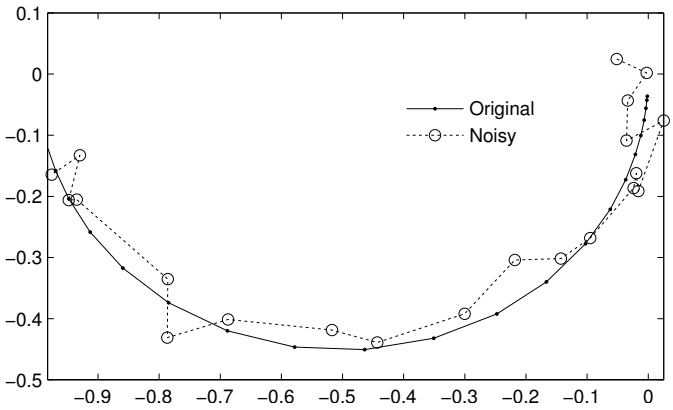

Figure 6: An instance of a frequency response added with a 25 dB AWGN.

3.3 Laboratory Data

The primary interest of this section is to examine the physical meaning of the estimated DSRF. It is shown here that the estimated spectrum agrees with the theoretical, physical DSRF derived from electromagnetic theory, and the estimate is not just another good fit to the data, which can be a problem for other estimation methods [7]. The data are measured with a wideband EMI sensor operating at 21 frequencies approximately logarithmically distributed over the range 300 Hz–90 kHz [30].

3.3.1 Single Loop

It is examined here the simplest case — a single thin wire circular loop. This target contains only one relaxation located at $\zeta = R/L$, where L is the inductance and R is the resistance of the loop. These quantities can be computed according to (26) and (27) in Appendix D. The theoretical EMI frequency response and DSRF can be found in [34].

Figure 7(a) shows three independently measured EMI responses for circular copper loops of circumferences 150, 200, 200 mm and AWG No. 24, 32, and 36, respectively. The theoretical and estimated DSRF are plotted together in Fig. 7(b). The estimates are seen to agree with the theory. The deviations from the theory are 0.0047, 0.0117, and 0.0028 decades for the loops with AWG No. 24, 32, and 36, respectively. All deviations are relatively small in the observable relaxation frequency range, and it can be concluded that the estimated DSRF is an accurate representation of the physical DSRF.

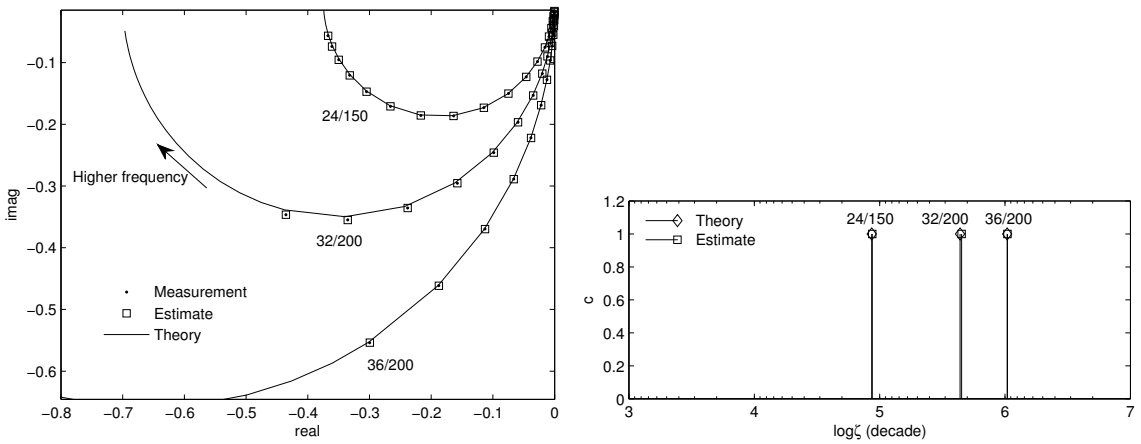

(a) (b)

Figure 7: (a) Frequency response of three independently measured single loops on an Argand diagram. Responses are normalized such that $\|\boldsymbol{h}\|_2 = 1$. Measurements are labeled in the form of AWG/circumference(mm). (b) Theoretical and estimated DSRF. Theoretical $\log \zeta_k$, from left to right, are 4.9364, 5.6416, and 6.0167. Estimated $\log \hat{\zeta}_l$, from left to right, are 4.9411, 5.6534, and 6.0195. All relaxations have an amplitude of unity.

3.3.2 Two Coplanar Coaxial Circular Loops

To test the method on a more complicated spectrum, the two-coplanar-coaxial-circular-loops target is reconsidered. A physical target was built according to the same specifications described in Section 3.2.1. The EMI response of this target was measured in the laboratory and is shown in Fig. 8(a). The SNR is about 70 dB. The estimated and theoretical DSRF are displayed in Fig. 8(b).

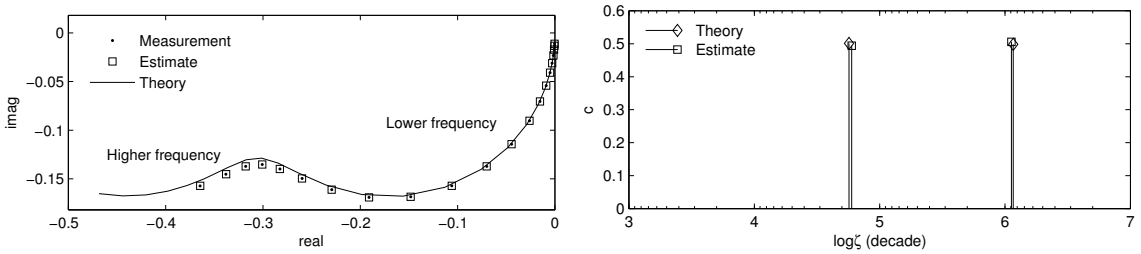

(a) (b)

Figure 8: (a) Laboratory measured frequency response of two coplanar coaxial circular loops on an Argand diagram. Theory deviates from the measurement at higher frequencies. Responses are normalized such that $\|\boldsymbol{h}\|_2 = 1$. (b) Theoretical and estimated DSRF. $\log \zeta_k$ and c_k are (4.7552 6.0651) and (0.5013 0.4987), respectively. The estimate $\log \hat{\zeta}_l$ and $\hat{c}_l$ are (4.7768 6.0514) and (0.4941 0.5059), respectively.

The estimated DSRF deviates from the theory slightly with a deviation of 0.0177 decades. This is most likely due to the thin-wire approximation used in the theory. In the theory, the wire radius is assumed to be much smaller than the loop radius. The inner loop (#22 AWG) has a loop radius to wire radius ratio of about of 47 which is not very high, meaning the wire cannot be modeled as infinitely thin. In addition, thicker wires have a secondary relaxation due to the off-wire-axial current flow which is not accounted for in the theory. At any rate, the deviation is small, and the estimated spectrum is very close to the theory. Thus, it can be concluded that this estimated DSRF is an accurate representation of the true DSRF of the physical target.

3.3.3 Non-magnetic Sphere

The spectrum of a metallic sphere is difficult to estimate because it contains an infinite sequence of relaxations, and the spacing between successive relaxation frequencies decreases as the relaxation frequency decreases [3]. The decrease in spacing makes the relaxations in the region of these closely spaced ζ indistinguishable from one another. It is therefore understood that it is impossible to perfectly recover the spectrum of a sphere. Here, the proposed method is tested against the EMI response of an aluminum sphere measured in the lab. The sphere has a radius of 0.9525 cm. The theoretical and estimated DSRF are plotted in Fig. 9. The EMD between the truth and estimate is 0.1088 decades.

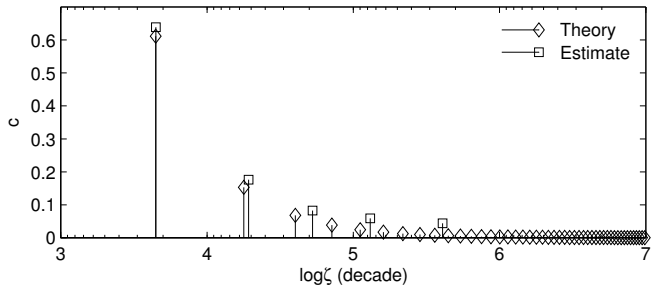

Figure 9: DSRF estimation of a laboratory-measured sphere. The theoretical DSRF has an infinite sequence of relaxation frequencies.

In the estimated DSRF, the first two relaxations are correctly recovered, but the remaining theoretical relaxations are accounted for by the other three estimated ones. It is observed that closely-spaced theoretical relaxations in one region are combined into one

estimated relaxation, and the theoretical spectral amplitudes in that region roughly add up to the estimated spectral amplitude. For example, the right-most estimated relaxation has an amplitude of 0.0438, and it accounts for the infinitely many theoretical relaxations to its right, which have an amplitude sum of 0.0521. The estimated DSRF, even though it cannot recover exactly the theoretical DSRF, is seen to approximate the theory. In this case of a sphere, the estimated DSRF is an approximation to the physical DSRF, and it is not just a good fit, but a fit that can be related to the physical properties of the target.

3.4 Field Data

As a final demonstration of the proposed method, it is estimated the DSRF of three types of landmines (Fig. 10). The EMI measurement system uses a dipole transmit coil and a quadrapole receive coil along with a down-track filter that is important to make the nonnegative constraint applicable for this system [30]. For each type of landmine, measurements were collected from several landmines buried at different depths and locations, and the DSRF of each sample was estimated and then plotted together with others of the same type. The spectral amplitudes are represented by the color intensity.

Figure 10(a) presents the DSRF of seven Type-A landmines: a low-metal content, nonmagnetic, moderate EMI response antipersonnel landmine. The SNR ranges from about 45 dB to 60 dB. All seven Type-A landmines exhibit consistency in the relaxation frequencies and the spectral amplitudes. The average EMD between pairs of landmines is 0.0594 decades.

Figure 10(b) presents the DSRF of eight Type-B landmines: a medium-metal content, magnetic, strong EMI response antipersonnel landmine. The SNR ranges from about 55 dB to 70 dB. The spectra are consistent, both $\hat{\boldsymbol{\zeta}}$ and $\hat{\boldsymbol{c}}$ exhibit the same behavior in all eight samples. Mine #7 differs from the others somewhat in $\hat{\boldsymbol{\zeta}}$, but the number of relaxations and the trend of spectral amplitudes is the same as the other seven Type-B landmines. The average EMD between pairs of landmines is 0.1536 decades.

Figure 10(c) presents the DSRF of seven Type-C landmines: a low-metal content, magnetic, weak EMI response antipersonnel landmine. The SNR ranges from about 20 dB to

35 dB. The spectra are less consistent compared to Type-A and Type-B landmines, but notice that the prominent relaxations are all located around logζ=5 decades. Since the response is weak, the noise could move the relaxations around as seen in Fig. 10(c). The average EMD between landmine pairs is 0.1490 decades, which is slightly lower than the average EMD in Fig. 10(b). This is because the two prominent relaxations in Fig. 10(b) are farther away from each other.

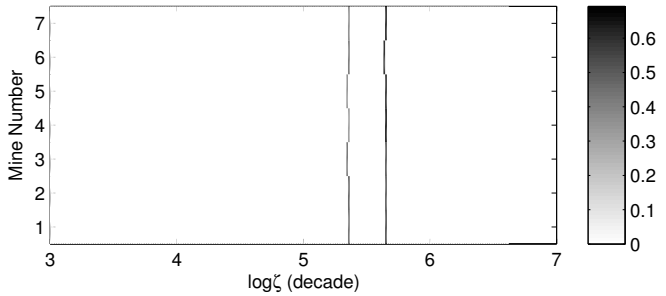

(a)

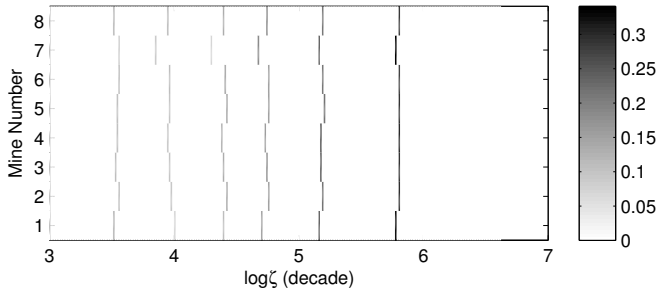

(b)

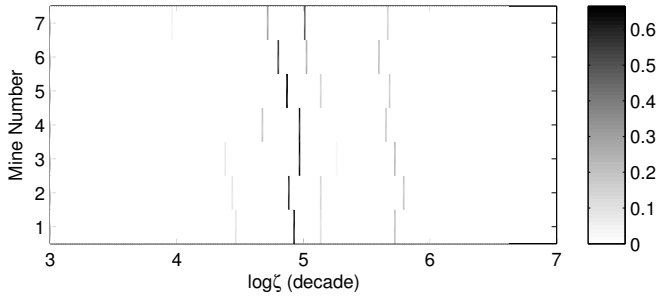

(c)

Figure 10: Estimated DSRF of real landmines. The spectral amplitude is represented by the intensity: darker the color, larger the amplitude. (a) Seven Type-A landmines. (b) Eight Type-B landmines. (c) Seven Type-C landmines.

The estimated $H(0)$ of the three types of landmines are normalized and plotted in

Fig. 11. The normalized $H(0)$ reflects the magnetic properties of the landmines. Type-A landmines are nonmagnetic and therefore have a normalized $H(0)$ close to zero. The other two types of landmines have a normalized $H(0)$ well above zero which reflects the magnetic content of the landmines. Variations in the estimated $H(0)$ are consistent with the variations in the DSRF.

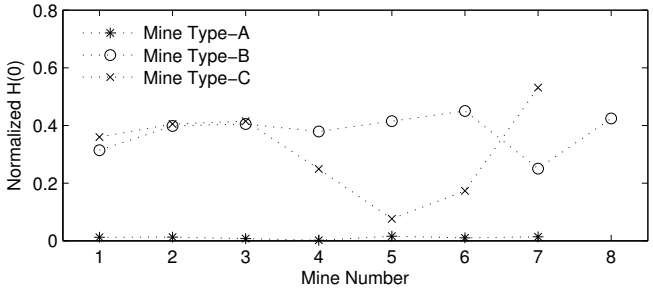

Figure 11: Normalized estimated $H(0)$ for landmines in Fig. 10. $H(0)$ is normalized by $\sum_{l=1}^{L} \hat{c}_l$.

The variation of the estimated DSRF and $H(0)$ could be caused by several factors such as manufacturing variations, corrosion, the magnetic properties of the soil, or measurement errors. Manufacturing variations in the shape of the metal parts and their electrical and magnetic properties can cause variations in the DSRF. Corrosion can change the properties of the metal parts which will change its response. It is possible that landmine #7 in Fig. 10(b) has a metal part slightly different from the other seven instances. The lower normalized $H(0)$ suggests a different magnetic property, and the slightly different DSRF reaffirms this small variation in the metal.

The response due to the magnetic properties of the soil can also influence the DSRF since the response of the soil is superimposed on the response of the target and it is not possible to completely separate the two. For the landmines presented in Fig. 10(c), the variation in the estimated $H(0)$ maybe primarily due to the magnetic properties of the soil. Since the magnetic shift observed in the response of the soil is on the same order of magnitude as the response of these landmines, the soil can have a strong influence on the landmine responses. On the other hand, landmines presented in Fig. 10(b) have much stronger EMI responses, and influence from the soil is therefore insignificant.

In general, landmine of one type have consistent estimated DSRFs. These stable and recurring DSRFs could be a valuable feature to be exploited in target discrimination. The estimated $H(0)$ can also be used as a feature when it is not overwhelmed by the noise or ground response.

3.4.1 Dissimilarity Between Various Mine Types

It is further demonstrated here the consistency of the estimated DSRF from targets of the same type and also the dissimilarity between different types of targets [36]. It is chosen one hundred independently measured field samples from eleven types of landmines and various metal clutter objects [30]. After estimating the DSRF of each sample, the EMD between all pairs of DSRFs is computed to generate the dissimilarity map shown in Fig. 12. The diagonal is zero because that is the EMD between a DSRF and itself which is zero.

It is seen that landmines of the same type are, in EMD units, close to each other, meaning landmines of the same type are similar. Mines of type **I** do not have small EMD among its sample pairs. The reason is unclear, but it is speculated that this target has negative relaxations as the real part of the responses do not always decrease with the frequency. Therefore, the estimated DSRF could be inaccurate. On the other hand, landmines and clutter, are far from each other, with few exceptions. Clutter that is similar to landmines may cause false alarms, but the EMD from clutter to any type of mine is mostly smaller than the EMD within that mine type. The plot simply shows the clustering of landmines and suggests the applicability of the DSRF for target discrimination.

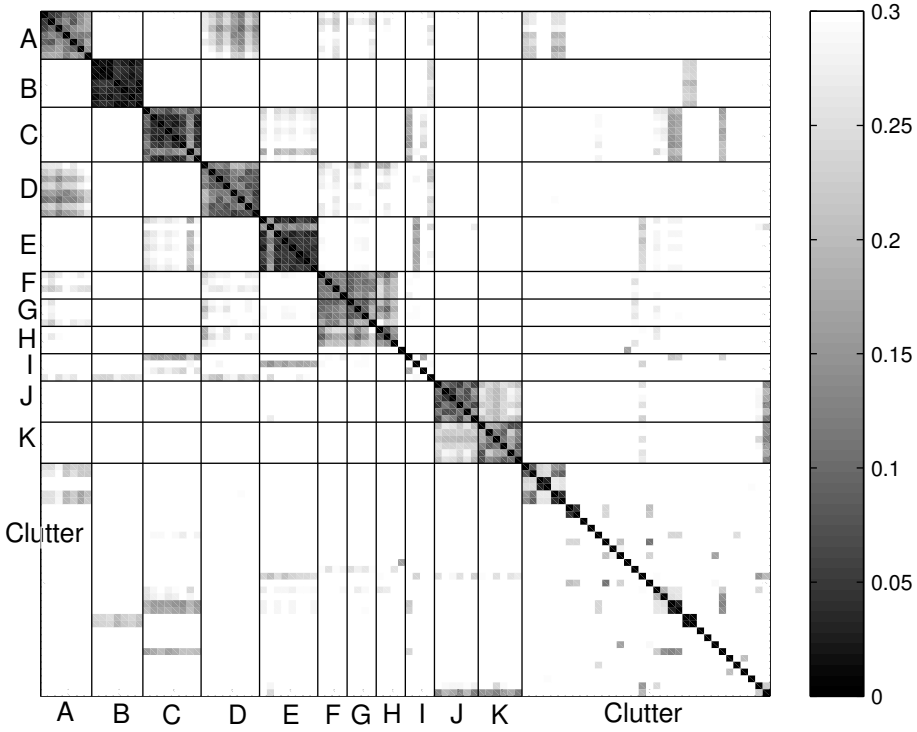

Figure 12: The EMD between samples from eleven types of landmines (A to K) and metal clutter. Darker colors denote smaller distances which indicate that two samples are more similar.

CHAPTER IV

CONCLUSIONS

In this thesis, a robust method is formulated to estimate the DSRF of a target. The proposed method does not require a priori knowledge of the model order and returns only real parameters. The proposed method is tested with a wide variety of data, targets, and noise levels, and is found to give stable, accurate, and quick estimates of the DSRF of a target. When the DSRF cannot be exactly recovered, the estimate is an approximation to the actual. In all cases, the estimated DSRF is directly related to the physical properties of the target.

The consistently estimated DSRF from targets of the same type suggests that the proposed method is a promising way to generate features for target discrimination. The rotational and positional invariability of the relaxation frequencies also suggests the potential of performing target discrimination using the DSRF. Designing a target discriminator based on the estimated DSRF would be a natural extension of this work.

APPENDIX A

THE EMI MODEL

The physical model of the EMI response and its relation to the DSRF model is presented here. The EMI response of a metallic object is the result of the interaction between the transmitting loops, the receiving loops, and the object's magnetic polarizability $\boldsymbol{M}$ [31]:

$$H(\omega) = \alpha {\mathrm{H_R}}^T \boldsymbol{M}(\omega) \mathrm{H_T}, \tag{12}$$

where α is a real constant, $\mathrm{H_T}$ is the magnetic field generated by the transmitting loop, $\mathrm{H_R}$ is the magnetic field of the receiving loop if it is driven, and $\boldsymbol{M}$ is a complex, frequency independent, second rank tensor.

Equation (12) can be expanded because the magnetic polarizability of a target can be written as a sum of relaxations [3]:

$$\boldsymbol{M}(\omega) = T_0 \boldsymbol{T}_0 - \sum_{k=1} T_k \left(\frac{j\omega/\zeta_k}{1 + j\omega/\zeta_k}\right) \boldsymbol{T}_k, \tag{13}$$

where T_k is a real constant and $\boldsymbol{T}_k$ is a real, symmetric, second rank tensor. The first term is due to the bulk magnetic permeability of the target, which is assumed to be frequency independent, and the second term is due to the currents induced in the target [31].

Expanding $\boldsymbol{M}$ in (12) using (13), the response becomes

$$\begin{aligned} H(\omega) &= \alpha {\mathrm{H_R}}^T \left[T_0 \boldsymbol{T}_0 - \sum_{k=1} T_k \left(\frac{j\omega/\zeta_k}{1 + j\omega/\zeta_k}\right) \boldsymbol{T}_k \right] \mathrm{H_T} \\ &= \alpha \left[T_0 {\mathrm{H_R}}^T \boldsymbol{T}_0 \mathrm{H_T} - \sum_{k=1} T_k \left(\frac{j\omega/\zeta_k}{1 + j\omega/\zeta_k}\right) {\mathrm{H_R}}^T \boldsymbol{T}_k \mathrm{H_T} \right] \\ &= d_0 - \sum_{k=1} d_k \frac{j\omega/\zeta_k}{1 + j\omega/\zeta_k}, \end{aligned} \tag{14}$$

where $d_k = \alpha T_k {\mathrm{H_R}}^T \boldsymbol{T}_k \mathrm{H_T}$, and it is noted that ${\mathrm{H_R}}^T \boldsymbol{T}_k \mathrm{H_T}$ is constant for a given position and orientation of the target relative to the sensors. This form provides more intuition of the physical process of the EMI, where, again, the first term is due to the bulk magnetic permeability of the target and the second term is due to the currents induced in the target.

The EMI model in (14) can be related to the model presented in Section 1.2 by

$$\begin{aligned}
H(\omega) &= d_0 - \sum_{k=1} d_k \frac{j\omega/\zeta_k}{1 + j\omega/\zeta_k} \\
&= d_0 - \sum_{k=1} d_k \frac{j\omega/\zeta_k}{1 + j\omega/\zeta_k} + d_k - d_k \\
&= \left(d_0 - \sum_{k=1} dk \right) - \sum_{k=1} d_k \frac{j\omega/\zeta_k}{1 + j\omega/\zeta_k} - d_k \frac{1 + j\omega/\zeta_k}{1 + j\omega/\zeta_k} \\
&= \left(d_0 - \sum_{k=1} dk \right) + \sum_{k=1} \frac{d_k}{1 + j\omega/\zeta_k} \\
&= c_0 + \sum_{k=1} \frac{c_k}{1 + j\omega/\zeta_k}.
\end{aligned}$$

It is identified that c_k and d_k are related by

$$d_k = c_k, \qquad k = 1, 2, 3, \ldots \tag{15}$$

$$d_0 = c_0 + \sum_{k=1} c_k. \tag{16}$$

APPENDIX B

NONNEGATIVE SPECTRUM

It is examined here the relation between the nonnegative spectral amplitudes and the observation that the real part of a frequency response decreases as the frequency increases. It is found that whenever the real part of a frequency response decreases with respect to the frequency, one can practically assume the spectral amplitudes are all nonnegative.

The EMI frequency response of a metallic target can be modeled as

$$H(\omega) = c_0 + \sum_{k=1}^{K} \frac{c_k}{1 + j\omega/\zeta_k}. \tag{17}$$

For a frequency response to have decreasing real part with respect to the frequency ω, it is sufficient but not necessary to have all nonnegative c_k, as shown in the derivation below. However, the derivation also suggests that whenever a c_k is negative it is either (a) very small in magnitude or (b) close to another positive c_k of larger magnitude, which makes this negative c_k practically nonnegative.

Suppose a response has two relaxations

$$H(\omega) = \frac{a}{1 + j\omega/\zeta_a} - \frac{b}{1 + j\omega/\zeta_b} \tag{18}$$

with $a, b > 0$. The real part of the response is

$$Re\{H(\omega)\} = \frac{a}{1 + \omega^2/\zeta_a^2} - \frac{b}{1 + \omega^2/\zeta_b^2}.$$

To have a decreasing real part with respect to the frequency, it must be satisfied that

$$\frac{dRe\{H(\omega)\}}{d\omega} = \frac{-2a\omega/\zeta_a^2}{(1 + \omega^2/\zeta_a^2)^2} + \frac{2b\omega/\zeta_b^2}{(1 + \omega^2/\zeta_b^2)^2} < 0. \tag{19}$$

Multiply by $(1 + \omega^2/\zeta_a^2)^2(1 + \omega^2/\zeta_b^2)^2/(2\omega)$:

$$-a\zeta_a^2(1 + \omega^2/\zeta_b^2)^2 + b\zeta_b^2(1 + \omega^2/\zeta_a^2)^2 < 0.$$

Express in the form $x^2 - y^2$:

$$\left[\sqrt{b}\zeta_b^{-1}(1 + \omega^2/\zeta_a^2)\right]^2 - \left[\sqrt{a}\zeta_a^{-1}(1 + \omega^2/\zeta_b^2)\right]^2 < 0.$$

Use the identity $x^2 - y^2 = (x+y)(x-y)$:

$$[\sqrt{b}\zeta_b^{-1}(1+\omega^2/\zeta_a^2) + \sqrt{a}\zeta_a^{-1}(1+\omega^2/\zeta_b^2)]\cdot$$
$$[\sqrt{b}\zeta_b^{-1}(1+\omega^2/\zeta_a^2) - \sqrt{a}\zeta_a^{-1}(1+\omega^2/\zeta_b^2)] < 0$$

The first term can be divided out because it is positive:

$$\sqrt{b}\zeta_b^{-1}(1+\omega^2/\zeta_a^2) - \sqrt{a}\zeta_a^{-1}(1+\omega^2/\zeta_b^2) < 0.$$

Rearrange in the powers of ω:

$$g(\omega) = \omega^2(\frac{\sqrt{a}}{\zeta_a\zeta_b^2} - \frac{\sqrt{b}}{\zeta_a^2\zeta_b}) + \frac{\sqrt{a}}{\zeta_a} - \frac{\sqrt{b}}{\zeta_b} > 0. \tag{20}$$

To satisfy (19) is to satisfy $g(\omega) > 0$. The following finds the minimum of $g(\omega)$ and ensures it is positive.

$$\frac{dg(\omega)}{d\omega} = 2\omega(\frac{\sqrt{a}}{\zeta_a\zeta_b^2} - \frac{\sqrt{b}}{\zeta_a^2\zeta_b}) = 0$$

The extremum is at $\omega = 0$. To have this extremum be a minimum,

$$\left.\frac{d^2g(\omega)}{d\omega^2}\right|_{\omega=0} = 2(\frac{\sqrt{a}}{\zeta_a\zeta_b^2} - \frac{\sqrt{b}}{\zeta_a^2\zeta_b}) > 0$$
$$\frac{\sqrt{a}}{\zeta_a\zeta_b^2} > \frac{\sqrt{b}}{\zeta_a^2\zeta_b}$$
$$\frac{a}{b} > \left(\frac{\zeta_b}{\zeta_a}\right)^2. \tag{21}$$

Restrict the minimum be positive:

$$g(\omega=0) = \frac{\sqrt{a}}{\zeta_a} - \frac{\sqrt{b}}{\zeta_b} > 0$$
$$\frac{\sqrt{a}}{\zeta_a} > \frac{\sqrt{b}}{\zeta_b}$$
$$\frac{a}{b} > \left(\frac{\zeta_a}{\zeta_b}\right)^2. \tag{22}$$

Therefore, $H(\omega)$ has decreasing real part with respect to ω when (21) and (22) are satisfied. Or equivalently,

$$\frac{a}{b} > max(\left(\frac{\zeta_a}{\zeta_b}\right)^2, \left(\frac{\zeta_b}{\zeta_a}\right)^2). \tag{23}$$

This also requires $a > b$ since the right-hand side ≥ 1.

To interpret this result, (23) is expressed in an alternative form. Take the log of (23) on both sides:

$$\frac{1}{2}\log\frac{a}{b} > |\log\zeta_a - \log\zeta_b|. \tag{24}$$

The right-hand side is the distance between the two relaxations in log space. When the negative component is relatively large (b large, $a/b \to 1$; recall that $a > b$) the left-hand side approaches zero and the distance approaches zero. When the negative component is far away from the positive one (right-hand side large), b is required to be relatively small to a. In either case, the negative relaxation would be overwhelmed by the positive relaxation, especially under the presence of noise.

A similar conclusion can be make about the imaginary part of a response is always negative. It is easy to prove that the nonnegative spectral amplitude is also a sufficient but not a necessary condition to having negative imaginary part. This proof is left as an exercise to the reader.

APPENDIX C

DENSITY OF DISCRETIZATION OF THE RELAXATION FREQUENCY SPACE

The number M in (5) decides the number of sample points placed in a relaxation frequency range. Equivalently, M controls the density of discretization of the ζ space. The denser the discretization, the more likely a sampled ζ is close to the true ζ. In the extreme case, if an infinite number of sample points fill up the relaxation frequency range, there must be one sampled ζ that coincides with the true ζ. Of course, computationally it would be impossible to estimate a DSRF with an infinite number of sample points. Even if the number of samples is kept finite, with a fixed number of observations N, the null space of $\tilde{\boldsymbol{Z}}$ gets larger and larger as M increases, and the number of possible bad estimates increases. It is therefore desirable to have M just large enough, so that the estimate is likely correct while the computational cost remains low.

To determine an good choice of M, a Monte Carlo simulation on the density of discretization of ζ space is performed over a range of M with different noise levels. The simulation result is shown in Fig. 13, where a higher EMD value means worse estimates. The figure suggests that M should be greater than 60 to avoid bad estimation due to insufficient sample points while M should be no greater than 200 because adding more sample points does not improve the goodness of fit. It is seen that within the range $60 < M < 200$, at lower signal-to-noise ratios (50–60 dB), better estimation is obtained with $M \approx 70$. While at higher SNRs (65–80 dB), better estimation is obtained with $M \approx 120$. In words, at lower SNR, lower discretization density gives more robust performance, which agrees with the intuition that larger dictionaries are more sensitive to perturbation of noise. On the other hand, when the SNR is high, higher discretization density delivers more accurate estimates. To accommodate a wide range of SNR, to chose $M \approx 100$ is a good compromise, and since the relaxation frequency range is about 4 decades, there are about 25 sample points per

decade.

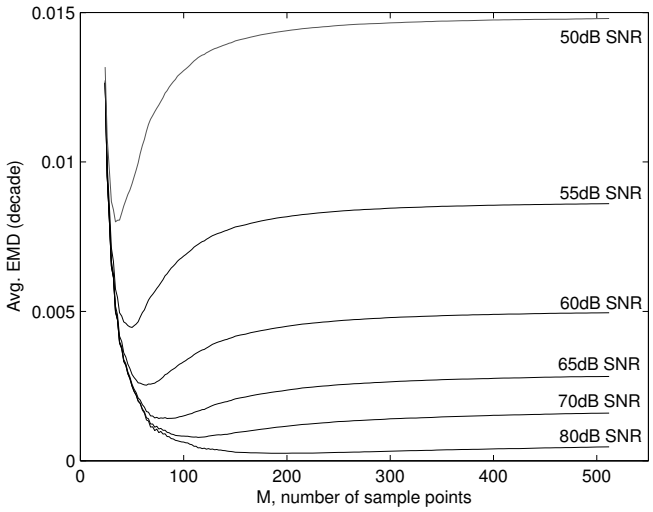

Figure 13: Monte Carlo simulation on density of discretization of ζ space. Each point on the curve is the average EMD over 10,000 samples.

Although the Monte Carlo simulation is performed on a two-relaxation target, the result should well represent the behavior of the estimation process in general. This is true as observed in simulations of different DSRF. Therefore, it can be inferred that, in general, a good choice of M is around 25 sample points per decade. As shown in the figure, the goodness of fit is not sensitive to the chosen M given it is large enough, so there is some freedom on choosing M.

APPENDIX D

A CIRCUIT MODEL FOR TWO COPLANAR COAXIAL CIRCULAR LOOPS

It is derived here a theoretical approximation to the magnetic polarizability of two coplanar coaxial circular loops in low-frequency realm. A larger loop of radius r_1 with wire radius a_1 is placed around a smaller loop of radius r_2 with wire radius a_2. The wires have electric conductivity σ and relative permeability μ_r. Two loops are on the same plane and share the same center. The wire radius is assumed to be much smaller than the loop radius. i.e., $a << r$. This configuration of two coplanar coaxial circular loops can be modeled as a simple two coupled LR circuits shown in Fig. 14.

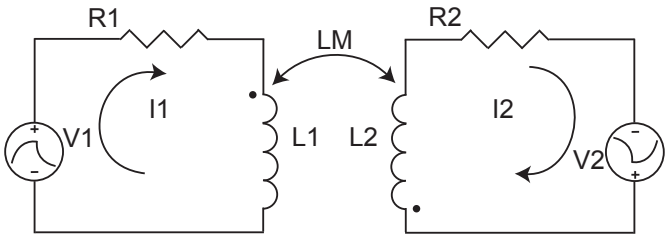

Figure 14: Circuit model for two coplanar coaxial circular loops.

The voltage $V(s)$ induced by the incident magnetic field on the loop is related to the incident magnetic excitation H^{inc} in Laplace domain through

$$V(s) = -s\mu_0 H^{inc} A, \tag{25}$$

where $\boldsymbol{A}$ is the loop area and μ_0 is the permeability of free space. Assume the incident magnetic field is normal to the plane containing the loops. In low frequency, the resistance R of the loop is

$$R = \frac{2r}{a^2\sigma}, \tag{26}$$

and the inductance L is [32]

$$L = r\mu_0[(1 + \frac{a^2}{8r^2})ln(\frac{8r}{a}) + \frac{a^2}{24r^2} - 2 + \frac{\mu_r}{4}]. \tag{27}$$

The mutual inductance L_M between the two loops is [33]

$$L_M = \frac{2\mu\sqrt{r_1 r_2}}{k}[(1 - \frac{1}{2}k^2)K(k) - E(k)], \tag{28}$$

where

$$k^2 = \frac{4r_1 r_2}{(r_1 + r_2)^2}, \tag{29}$$

and K and E are the complete elliptic integrals.

In the Laplace domain, the system equation for the circuit is [34]

$$\begin{bmatrix} V_1 \\ V_2 \end{bmatrix} = \begin{bmatrix} R_1 + sL_1 & sL_M \\ sL_M & R_2 + sL_2 \end{bmatrix} \begin{bmatrix} I_1 \\ I_2 \end{bmatrix}. \tag{30}$$

Solve for the currents:

$$\begin{bmatrix} I_1 \\ I_2 \end{bmatrix} = \frac{-s\mu_0 H^{inc}}{(R_1 + sL_1)(R_2 + sL_2) - (sL_M)^2} \cdot \begin{bmatrix} R_2 + sL_2 & -sL_M \\ -sL_M & R_1 + sL_1 \end{bmatrix} \begin{bmatrix} A_1 \\ A_2 \end{bmatrix}. \tag{31}$$

The magnetic polarizability $\boldsymbol{M}$ is then

$$\boldsymbol{M}(s) = \frac{A_1 I_1 + A_2 I_2}{H^{inc}} \tag{32}$$

$$= \frac{-s\mu_0[A_1^2(R_2 + sL_2) + A_2^2(R_1 + sL_1) - 2sA_1A_2L_M]}{(R_1 + sL_1)(R_2 + sL_2) - (sL_M)^2}. \tag{33}$$

Perform partial fraction expansion:

$$\boldsymbol{M}(s) = -s(\frac{Q_1}{s - s_1} + \frac{Q_2}{s - s_2}) \tag{34}$$

$$= -(Q_1 + Q_2) + \frac{Q_1}{1 - s/s_1} + \frac{Q_2}{1 - s/s_2}, \tag{35}$$

where s_1 and s_2 are the roots of the denominator in (33) [12]:

$$s_{1,2} = \frac{-(R_1L_2 + R_2L_1) \pm \sqrt{(R_1L_2 - R_2L_1)^2 + 4R_1R_2L_M^2)}}{2(L_1L_2 - L_M^2)}. \tag{36}$$

Variable Q_1 and Q_2 are simply

$$Q_1 = \frac{\mu_0[A_1^2(R_2 + s_1L_2) + A_2^2(R_1 + s_1L_1) - 2s_1A_1A_2L_M]}{s_1 - s_2} \tag{37}$$

$$Q_2 = \frac{\mu_0[A_1^2(R_2 + s_2L_2) + A_2^2(R_1 + s_2L_1) - 2s_2A_1A_2L_M]}{s_2 - s_1}. \tag{38}$$

Using (36)–(38) the DSRF of two coplanar coaxial circular loops can be computed. The relaxation frequency $\zeta_k = -s_k$ with corresponding spectral amplitude Q_k.

APPENDIX E

EARTH MOVER'S DISTANCE

Given two distributions $\hat{S} = \{(\hat{\zeta}_i, \hat{c}_i) : i = 1 \dots L\}$ and $S = \{(\zeta_j, c_j) : j = 1 \dots K\}$, the Earth Mover's Distance (EMD) between the two distributions can be computed by solving the optimization problem [10]:

$$\text{Define } d_{ij} = |\log \hat{\zeta}_i - \log \zeta_j| \tag{39}$$

$$\text{EMD}(\hat{S}, S) = \min_{f_{ij}} \frac{\sum_{i=1}^{L} \sum_{j=1}^{K} f_{ij} d_{ij}}{\sum_{i=1}^{L} \sum_{j=1}^{K} f_{ij}} \tag{40}$$

$$\text{subject to} \quad \sum_{j=1}^{K} f_{ij} \leq \hat{c}_i \quad i = 1 \dots L \tag{41}$$

$$\sum_{i=1}^{L} f_{ij} \leq c_j \quad j = 1 \dots K \tag{42}$$

$$\sum_{i=1}^{L} \sum_{j=1}^{K} f_{ij} = \min(\sum_{i=1}^{L} \hat{c}_i, \sum_{j=1}^{K} c_j) \tag{43}$$

$$f_{ij} \geq 0 \quad i = 1 \dots L, \, j = 1 \dots K \tag{44}$$

where f_{ij} is an intermediate variable used during the optimization. Adapting the illustration in Section 3.1, $\hat{S}$ is the piles of earth and S the holes. Equation (41) guarantees no overdraw from each pile of earth, (42) guarantees no over fill at each hole, (43) sets the problem to fill up the holes with as much earth as possible, and (44) allows only moving earth into holes and not the reverse.

In this work, spectra should be normalized having sum of all spectral amplitudes be unity ($\sum c_i = 1$). In this case, the above optimization problem is simplified to having the denominator in (40) be one and the right-hand-side of (43) be unity. The EMD also becomes symmetric.

REFERENCES

[1] Barsoukov, E. and Macdonald, J. R., *Impedance spectroscopy*, ch. 2, p. 37. New Jersey: Wiley-Interscience, 2005.

[2] Baum, C. E., "On the singularity expansion method for the solution of electromagnetic interaction problems," Interaction Notes 88, Air Force Weapons Laboratory, 1971.

[3] Baum, C. E., "Low-frequency near-field magnetic scattering from highly, bu not perfectly, conducting bodies," in *Detection and Identification of Visually Obscured Targets* (Baum, C. E., ed.), ch. 6, pp. 163–218, Philadelphia, PA: Taylor & Francis, 1999.

[4] Chen, S. S., Donoho, D. L., and Saunders, M. A., "Atomic decomposition by basis pursuit," *SIAM Review*, vol. 43, no. 1, pp. 129–159, 2001.

[5] Cole, K. S. and Cole, R. H., "Dispersion and absorption in dielectrics i. alternating current characteristics," *J. Chem. Phys.*, vol. 9, pp. 341–351, Apr. 1941.

[6] Collins, L., Gao, P., and Carin, L., "An improved Bayesian decision theoretic approach for land minedetection," *IEEE Trans. Geosci. Remote Sens.*, vol. 37, pp. 811–819, Mar. 1999.

[7] Das, Y. and McFee, J. E., "Limitations in identifying objects from their time-domain electromagnetic induction response," in *Proc. SPIE*, vol. 4742, (Orlando, FL), pp. 776–788, Apr. 2002.

[8] Davidson, D. W. and Cole, R. H., "Dielectric relaxation in glycerol, propylene glycol, and n-propanol," *J. Chem. Phys.*, vol. 19, pp. 1484–1490, Dec. 1951.

[9] Fails, E. B., Torrione, P. A., Scott, Jr., W. R., and Collins, L. M., "Performance of a four parameter model for modeling landmine signatures in frequency domain wideband electromagnetic induction detection systems," in *Proc. SPIE*, vol. 6553, (Orlando, FL), p. 65530D, Apr. 2007.

[10] Fisher, B., "The earth mover's distance," Oct. 2008.

[11] Gao, P., Collins, L., Garber, P. M., Geng, N., and Carin, L., "Classification of landmine-like metal targets using wideband electromagnetic induction," *IEEE Trans. Geosci. Remote Sens.*, vol. 38, pp. 1352–1361, May 2000.

[12] Geng, N., Baum, C. E., and Carin, L., "On the low-frequency natural response of conducting and permeabletargets," *IEEE Trans. Geosci. Remote Sens.*, vol. 37, pp. 347–359, Jan. 1999.

[13] Grant, F. S. and West, G. F., *Interpretation Theory in Applied Geophysics*, ch. 17. New York: McGraw-Hill, 1965.

[14] Grant, M., Boyd, S., and Ye, Y., "CVX: Matlab software for disciplined convex programming," July 2008.

[15] Hansen, P. C., *Rank-Deficient and Discrete Ill-Posed Problems: Numerical Aspects of Linear Inversion*. Philadelphia, PA: Society for Industrial Mathematics, 1998.

[16] Havriliak, S. and Negami, S., "A complex plane representation of dielectric and mechanical relaxation processes in some polymers," *Polymer*, vol. 8, pp. 161–210, 1967.

[17] Holmström, K. and Petersson, J., "A review of the parameter estimation problem of fitting positive exponential sums to empirical data," *App. Math. and Comp.*, vol. 126, pp. 31–61, Feb. 2002.

[18] Honerkamp, J. and Weese, J., "A nonlinear regularization method for the calculation of relaxation spectra," *Rheol. Acta*, vol. 32, pp. 65–73, 1993.

[19] International Campaign to Ban Landmines, *Landmine Monitor 2010*. Ottawa: Mines Action Canada, 2010.

[20] Kaufman, A. A. and Eaton, P. A., *The theory of inductive prospecting*, ch. 3. Amsterdam: Elsevier, 2001.

[21] Keiswetter, D. A., Won, I. J., Miller, J., Bell, T., Cespedes, E., and O'Neill, K., "Discriminating capabilities of multifrequency EMI data," in *Proc. IGARSS*, vol. 4, (Honolulu, HI), pp. 1415–1417, July 2000.

[22] Lawson, C. L. and Hanson, R. J., *Solving Least Squares Problems*, ch. 23. Englewood Cliffs, NJ: Prentice-Hall, Inc., 1974.

[23] Levy, E. C., "Complex-curve fitting," *IRE Trans. Automat. Contr.*, vol. 4, pp. 37–43, 1959.

[24] Miller, J. T., Bell, T. H., Soukup, J., and Keiswetter, D., "Simple phenomenological models for wideband frequency-domain electromagnetic induction," *IEEE Trans. Geosci. Remote Sens.*, vol. 39, pp. 1294–1298, June 2001.

[25] Osborne, M. R. and Smyth, G. K., "A modified Prony algorithm for exponential function fitting," *SIAM J. Sci. Comp.*, vol. 16, no. 1, pp. 119–138, 1995.

[26] Ramachandran, G., Gader, P. D., and Wilson, J. N., "Granma: Gradient angle model algorithm on wideband EMI data for land-mine detection," *IEEE Geosci. Remote Sens. Lett.*, vol. 7, no. 3, pp. 535–539, 2010.

[27] Riggs, L. S., Mooney, J. E., and Lawrence, D. E., "Identification of metallic mine-like objects using low frequency magnetic fields," *IEEE Trans. Geosci. Remote Sens.*, vol. 39, pp. 56–66, Jan. 2001.

[28] Rubner, Y., Tomasi, C., and Guibas, L. J., "A metric for distributions with applications to image databases," in *Proc. ICCV*, (Bombay, India), pp. 59–66, Jan. 1998.

[29] Sarkar, T. K. and Pereira, O., "Using the matrix pencil method to estimate the parameters of a sum of complex exponentials," *IEEE Antennas Propag. Mag.*, vol. 37, pp. 48–55, Feb. 1995.

[30] Scott, Jr., W. R., "Broadband array of electromagnetic induction sensors for detecting buried landmines," in *Proc. IGARSS*, (Boston, MA), July 2008.

[31] Scott, Jr., W. R. and Larson, G. D., "Modeling the measured em induction response of targets as a sum of dipole terms each with a discrete relaxation frequency," in *Proc. IGARSS*, (Honolulu, Hawaii), July 2010.

[32] Smythe, W. R., Silver, S., Whinnery, J. R., and Angelakos, D. J., "Electricity and magnetism," in *American Institute of Physics Handbook* (Gray, D. E., ed.), ch. 5, p. 29, NY: McGraw-Hill Book Company, Inc., 1963.

[33] Smythe, W. R., *Static and Dynamic Electricity*, ch. 8, p. 335. NY: McGraw-Hill, 1968.

[34] Sower, G. D., "Eddy current responses of canonical metallic targets theory and measurements," Interaction Notes 526, EG&G MSI, May 1997.

[35] Ward, S. H., "Electromagnetic theory for geophysical applications," in *Mining Geophysics* (Hansen, D. A., Heinrichs, Jr., W. E., Holmer, R. C., MacDougall, R. E., Rogers, G. R., Sumner, J. S., and Ward, S. H., eds.), vol. 2, ch. 2, pp. 10–196, Tulsa, OK: The Society of Exploration Geophysicists, 1967.

[36] Wei, M., Scott, Jr., W. R., and McClellan, J. H., "Estimation and application of discrete spectrum of relaxations for electromagnetic induction responses," in *Proc. IGARSS*, (Cape Town, South Africa), July 2009.

[37] Wei, M., Scott, Jr., W. R., and McClellan, J. H., "Robust estimation of the discrete spectrum of relaxations for electromagnetic induction responses," *IEEE Trans. Geosci. Remote Sens.*, vol. 48, pp. 1169–1179, Mar. 2010.